Optimal actuation of flagellar magnetic microswimmers

Yacine El Alaoui-Faris

Université Côte d'Azur, Inria, CNRS, LJAD, McTAO team, 06902 Nice, France
and Sorbonne Université, CNRS, ISIR, 75005 Paris, France

Jean-Baptiste Pomet ⓘ
Université Côte d'Azur, Inria, CNRS, LJAD, McTAO team, 06902 Nice, France

Stéphane Régnier
Sorbonne Université, CNRS, ISIR, 75005 Paris, France

Laetitia Giraldi ⓘ
Université Côte d'Azur, Inria, CNRS, LJAD, McTAO team, 06902 Nice, France

We present an automated procedure for the design of optimal actuation for flagellar magnetic microswimmers based on numerical optimization. Using this method, a magnetic actuation method is provided which allows these devices to swim significantly faster compared to the usual sinusoidal actuation. This leads to a novel swimming strategy which makes the swimmer perform a three-dimensional figure-eight trajectory. This shows that a faster propulsion is obtained when the swimmer is allowed to go out of plane. This approach is experimentally validated on a scaled-up flexible swimmer.

I. INTRODUCTION

Untethered robotic microswimmers have the potential to make a serious impact on the development of new promising therapeutic techniques [1–7]. However, due to their microscopic size, controlling their navigation through fluids inside the body faces numerous challenges [8,9]. These devices can take different shapes and designs (helicoidal [3,10,11], beating flexible tail [12,13], 2-linked structure [14], ciliary microrobots [15], etc.) and are actuated using multiple methods like chemical fuel propulsion [16,17], acoustic-based actuation [18], or external magnetic fields [1,19]. In this paper, we focus on sperm cell-inspired robotic swimmers composed of a magnetic head and an elastic tail and actuated by external magnetic fields [13,20]. As far as we know, the most commonly used actuation method for these swimmers is sinusoidal actuation. This consists in applying the superposition of a static orientating magnetic field parallel to the desired swimming direction and a perpendicular sinusoidal field that induces a planar symmetric beating of the tail, allowing a displacement along the swimming direction [21]. The purpose of this paper is to propose an automatic design method for the actuation of flexible magnetic microrobots that optimizes the swimming speed. The aim of this work is twofold: first, to provide a more efficient alternative to the commonly used sinusoidal actuation, and, second, to present an optimal control design method than can be adapted to deal with more demanding tasks, like swimming in a complex environment. Our method is based on the resolution of an optimal control problem under the constraints of an approximate dynamical model of the swimmer's displacement. In particular, we focus on computing a magnetic field shape

that maximizes the horizontal swimming speed of these devices. This actuation pattern is experimentally validated on a scaled-up flexible magnetic swimmer and compared to the classical sinusoidal actuation. The key for this approach is the use of a dynamical model that is sufficiently computationally inexpensive to be used as a constraint for an optimization process but still accurate enough to predict the displacement of a real-life low-Reynolds-number swimmer. For this purpose, we use a three-dimensional (3D) simplified dynamic model based on the approximation of the hydrodynamical forces using resistive force theory, [22,23] and the discretization of the curvature and elasticity of the tail of the swimmer, generalizing the planar "N-Link" models of Refs. [24–26]. Using this dynamic model as a constraint, the optimal control problem is numerically solved with a direct method using the software ICLOCS [27]. This results in a magnetic actuation pattern that induces a significantly faster propulsion than the common sinusoidal actuation. The optimal magnetic field has two time-varying components which makes the trajectory of the swimmer nonplanar. In particular, the optimal swimming strategy is to perform a 3D "figure-eight" trajectory around the swimming direction. This indicates the importance of going out of plane in order to maximize the propulsion speed of flexible swimmers. The optimal actuation is experimentally validated on a scaled-up flexible magnetic swimmer using a similar setting as in Ref. [20] and compared to the sinusoidal field. The horizontal displacement of the experimental swimmer is accurately predicted by the dynamic model for both fields. These results show the usefulness of the simplified swimmer model for the design of optimal controls that are usable in experiments.

FIG. 1. Experimental setup [20]. The three orthogonal Helmholtz coils generate a homogeneous magnetic field in the center, where the swimmer has been placed. The swimmer is tracked using two perpendicular cameras. In the corner: Scaled-up flexible magnetic swimmer used in the experiments.

II. EXPERIMENTAL SETTING

The flexible swimmer used in experiments consists of magnetic disk (neodyminum-iron-boron permanent magnet) with 0.3 mm in height and 0.77 mm in diameter attached to a silicone tail with 7 mm in length and 1 mm in diameter (see Fig. 1). The swimmer is immersed in pure glycerol to ensure low-Reynolds-number conditions ($\approx 10^{-2}$). It is placed at the center of three orthogonal Helmholtz coil pairs that generate the actuating magnetic field. Each pair of coils is driven by a servoamplifier (Maxon Motor) which outputs a constant current for a fixed input voltage. Two cameras provide a side view and a top view of the swimmer, and its position in 3D is tracked in real time using Visp software [28]. More information on the experimental setting used can be found in Refs. [20,29].

We consistently use a fixed frame (x, y, z) where the z axis is vertical and the y axis is along the axis of the side camera. In what follows, the desired swimming direction will be along the x axis.

The propulsion of the experimental swimmer is characterized by measuring its velocity-frequency response [given by the dotted line in Fig. (3)] under a magnetic field of the form:

$$\boldsymbol{B}(t) = [B_x \quad B_y \sin(2\pi f t) \quad 0]^T, \tag{1}$$

where $B_x = 2.5$ mT and $B_y = 10$ mT.

III. MODELING OF THE SWIMMER

A simplified dynamical model of the swimmer is used to simulate the swimmer's displacement under a three-dimensional magnetic field. The hydrodynamic effects on the swimmer are approximated by resistive force theory [22] and the shape of the tail is discretized into an articulated chain of N rigid slender rods, as done in the planar swimmer models of [24–26].
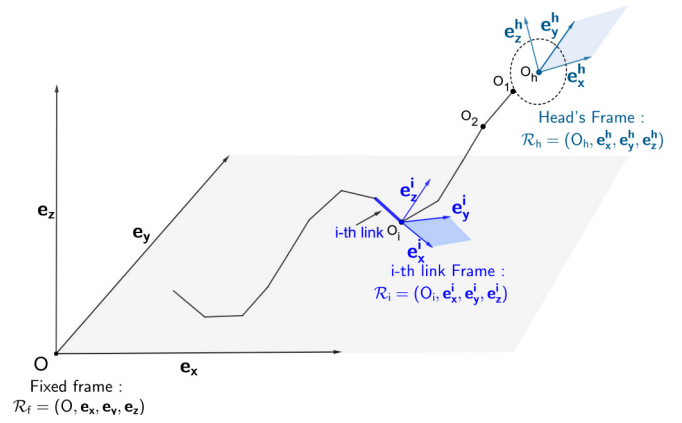
FIG. 2. Reference and local frames of the discrete-shape model. The swimmer's head frame is oriented relative to the reference frame. For each link i, the corresponding local frame $\mathcal{R}_i$ is oriented relative to $\mathcal{R}_h$.

A. Kinematics of the swimmer

We consider a moving frame $\mathcal{R}_{\text{head}} = (O_h, \boldsymbol{e}_x^h, \boldsymbol{e}_y^h, \boldsymbol{e}_z^h)$ associated to the head of the swimmer, where O_h is the center of the head. The orientation of each link i is represented by the moving frame $\mathcal{R}_i = (O_i, \boldsymbol{e}_x^i, \boldsymbol{e}_y^i, \boldsymbol{e}_z^i)$, where O_i is the extremity of the ith link. We call $R_{\text{head}} \in SO(3)$ the rotation matrix that allows the transformation of coordinates from the fixed reference frame to $\mathcal{R}_{\text{head}}$. Similarly, the matrix $R_i \in SO(3)$, for $i = 1 \cdots N$, denotes the relative rotation matrix that transforms coordinates from $\mathcal{R}_{\text{head}}$ to $\mathcal{R}_i$. We use the angles $(\theta_x, \theta_y, \theta_z)$ resulting from a $(Z\text{-}X\text{-}Y)$ rotation sequence to parametrize R_{head}. Since each link is considered to be slender and axisymmetric, the vectors $\boldsymbol{e}_y^i$ and $\boldsymbol{e}_z^i$ are only defined up to one rotation around, and hence we parametrize each matrix R_i by only two angles (ϕ_y^i, ϕ_z^i), resulting from a $Z\text{-}Y$ rotation sequence relative to the head frame.

With these notations, the swimmer is described by two sets of variables: The six *position variables*: $(\boldsymbol{X}, \boldsymbol{\Theta})$, where

$$X = (x_h, y_h, z_h) \in \mathbb{R}^3 \text{ and}$$
$$\Theta = (\theta_x, \theta_y, \theta_z) \in [0, \ 2\pi]^3, \tag{2}$$

and the 2N *shape variables*, denoted by

$$\boldsymbol{\Phi} = \left(\phi_y^1, \phi_z^1, \ldots, \phi_y^N, \phi_z^N \right). \tag{3}$$

The parametrization of the swimmer is shown in Fig. 2.

B. Dynamics of the swimmer

We assume that the swimmer is immersed in an unbounded domain of a viscous fluid. Due to its scale, we consider that the swimmer moves at low Reynolds number, i.e., that viscosity prevails over inertia and thus that the fluid is governed by Stokes equations. In what follows, the hydrodynamical interactions between the fluid and the swimmer are further simplified by using the resistive force theory (RFT) framework [22], where the interactions on the global scale between a slender Stokesian swimmer and the surrounding fluid are neglected in favor of the local anisotropic friction of the surface of the slender body with the nearby fluid. This results in explicit

expressions of the density of force applied by the fluid to the swimmer that are linear with respect to the velocities, hence to $(\dot{X}, \dot{\boldsymbol{\Theta}}, \dot{\boldsymbol{\Phi}})$.

From the integration of the local hydrodynamic force densities on each link, we are able to obtain the expression of $\boldsymbol{F}_{\mathbf{head}}^{h}$ and $\boldsymbol{F}_{i}^{h}$, the hydrodynamic drag forces on the head of the swimmer and on each link $i \in (1, \ldots, N)$ respectively. The expressions for $\boldsymbol{T}_{head,P}^{h}$ and $\boldsymbol{T}_{i,P}^{h}$, the moments of these forces about any given point P, are similarly derived from the local drag densities. We consider that the head of the swimmer is magnetized along the e_x^h axis. Denoting by $\boldsymbol{M}$ the magnetization vector of the head and considering an external homogeneous time-varying field $\boldsymbol{B}(t)$, the following torque is applied to the swimmer:

$$\boldsymbol{T}^{\mathbf{mag}} = \boldsymbol{M} \times \boldsymbol{B}(t). \tag{4}$$

The acceleration terms in the dynamics are neglected due to the low-Reynolds-number assumption [30], and, thus, the balance of forces and torques applied on the swimmer gives:

$$\begin{cases} \boldsymbol{F}_{\mathbf{head}}^{h} + \sum_{i=1}^{N} \boldsymbol{F}_{i}^{h} = 0_3 \\[2em] \boldsymbol{T}_{\mathbf{head}}^{h} + \sum_{i=1}^{N} \boldsymbol{T}_{i,H}^{h} = -\boldsymbol{T}^{\mathbf{mag}} \end{cases}, \tag{5}$$

which leads to six independent equations. In addition to these equations, the internal contributions of the tail are taken into account by adding the balance of torque on each subsystem consisting of the chain formed by the links i to N for $i = (1 \cdots N)$. These additional $3N$ equations reduce to $2N$ nontrivial equations by taking only the components perpendicular to the link k when calculating the sum of the torques from k to N. The elasticity of the tail is discretized by considering a restoring elastic moment $\boldsymbol{T}_i^{\mathbf{el}}$ at each joint O_i that tends to align each pair $(i, i+1)$ of adjacent links with each other:

$$\boldsymbol{T}_{i}^{\mathbf{el}} = k_{\mathrm{el}} e_x^i \times e_x^{i-1}. \tag{6}$$

Thus, the dynamics of the swimmer are described by the following system of $2N + 6$ equations:

$$\begin{cases} \boldsymbol{F}_{\mathbf{head}}^{h} + \sum_{i=1}^{N} \boldsymbol{F}_{i}^{h} = 0_3 \\[1.5em] \boldsymbol{T}_{\mathbf{head}}^{h} + \sum_{i=1}^{N} \boldsymbol{T}_{i,H}^{h} = -\boldsymbol{T}^{\mathbf{mag}} \\[1.5em] \sum_{i=1}^{N} \boldsymbol{T}_{i,1}^{h} . e_y^1 = -\boldsymbol{T}_1^{\mathbf{el}} \cdot e_y^1 \\[1.5em] \sum_{i=1}^{N} \boldsymbol{T}_{i,1}^{h} . e_z^1 = -\boldsymbol{T}_1^{\mathbf{el}} \cdot e_z^1 \\[1em] \vdots \\[0.5em] \boldsymbol{T}_{N,N}^{h} . e_y^n = -\boldsymbol{T}_n^{\mathbf{el}} \cdot e_y^n \\[0.5em] \boldsymbol{T}_{N,N}^{h} . e_z^n = -\boldsymbol{T}_n^{\mathbf{el}} \cdot e_z^n \end{cases}. \tag{7}$$

Following resistive force theory, the hydrodynamic contributions (left-hand side of the previous system) are linear with
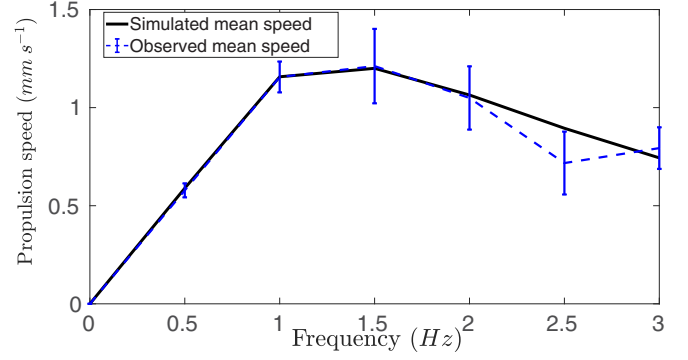
FIG. 3. Experimental ($N = 6$) and simulated horizontal swimming velocities for the frequency range $f = (0 \cdots 3 \text{ Hz})$.

respect to the rotational and translational velocities, thus, the previous system can be rewritten matricially in the form:

$$M^h(\boldsymbol{\Theta}, \boldsymbol{\Phi}) \begin{pmatrix} \dot{X} \\ \dot{\boldsymbol{\Theta}} \\ \dot{\boldsymbol{\Phi}} \end{pmatrix} = B(X, \boldsymbol{\Theta}, \boldsymbol{\Phi}), \tag{8}$$

where $M^h(\boldsymbol{\Theta}, \boldsymbol{\Phi})$ is a $2N + 6 \times 2N + 6$ matrix. The left-hand side of the equation represents the hydrodynamic effects on the swimmer and the right-hand side $B(X, \boldsymbol{\Theta}, \boldsymbol{\Phi})$ is the magnetic and elastic contributions on the swimmer. We refer the reader to the Appendix A for the full derivation of the matrix M^h. The previous equation can be rewritten as a control system where the dynamics of the swimmer are affine with respect to the components of the actuating magnetic field viewed as a control:

$$\begin{pmatrix} \dot{X} \\ \dot{\boldsymbol{\Theta}} \\ \dot{\boldsymbol{\Phi}} \end{pmatrix} = \boldsymbol{F}_0(\boldsymbol{\Theta}, \boldsymbol{\Phi}) + [B_x(t)\, B_y(t)\, B_z(t)] \begin{bmatrix} \boldsymbol{F}_1(\boldsymbol{\Theta}, \boldsymbol{\Phi}) \\ \boldsymbol{F}_2(\boldsymbol{\Theta}, \boldsymbol{\Phi}) \\ \boldsymbol{F}_3(\boldsymbol{\Theta}, \boldsymbol{\Phi}) \end{bmatrix}, \tag{9}$$

where the vector fields $F_0, \ldots, F_3$ are functions of the columns of $(M^h)^{-1}$ and of the magnetic and elastic constants.

C. Parameter identification

The hydrodynamic parameters (RFT coefficients) and the elasticity coefficient of the model are identified by nonlinear fitting to match the observed velocity-frequency response curve of the experimental swimmer under sinusoidal actuation. Three links were used for the approximation of the tail. Figure 3 shows the agreement between the experimental and simulated frequency responses. The fitted parameter values are given in Table I.

It is worth noting that using a finer discretization (more than three) of the tail only marginally improves the fitting error while adding to the computational cost of the magnetic field optimization, as it is shown in Fig. 9.

IV. MAGNETIC FIELD OPTIMIZATION

In what follows we focus on finding the time-varying magnetic field that maximizes the mean horizontal propulsion speed of the swimmer under the constraint of a periodic deformation. The admissible controls are of the form $(B_x, B_y(t), B_z(t))$, where the static orientating field B_x is
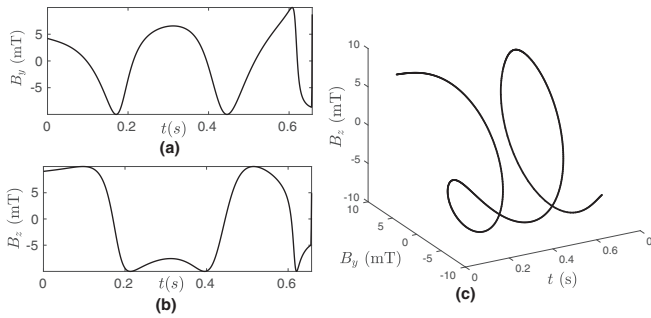
FIG. 4. Actuating magnetic field that maximizes the horizontal speed of the swimmer. Panels (a) and (b) are respectively the y and z components of the magnetic field. (c) Shape of the actuating *optimal* magnetic field deriving from the optimization process during one period.

fixed and the two dimensional time-varying actuating field $(B_y(t), B_z(t))$ is optimized. The bounds on the orientating field and the time-varying fields are taken to be the same as the sinusoidal field used in the experiments ($B_x = 2.5$ mT and $||(B_y(t), B_z(t))|| < 10$ mT). The deformation period is chosen to be the same as the observed optimal period for a sinusoidal actuation and it is imposed that the swimmer returns in its initial orientation and position on the y and z axes at the end of the period. This optimal control problem is numerically solved with the direct solver ICLOCS [27]. Figure 4 shows the result of the numerical optimization, where we can see the y [Fig. 4(a)] and z [Fig. 4(b)] components of the optimal magnetic field. Interestingly enough, this results in a simple magnetic field shape, shown in Fig. 4(c), where the actuating strategy over one deformation period is a partial rotation (about two thirds of a circle) of the magnetic field followed by a full rotation in the opposite direction. Repeating this pattern over time makes the swimmer revolve around the x axis, drawing a figure eight in the y-z plane. Figure 5 shows the simulated optimal trajectory of the swimmer compared to the trajectory under the sinusoidal field. The simulated fields perform better (mean propulsion speed of 1.45×10^{-3} ms^{-1}) than the sinusoidal actuation (mean propulsion speed of 1.2×10^{-3} ms^{-1}).
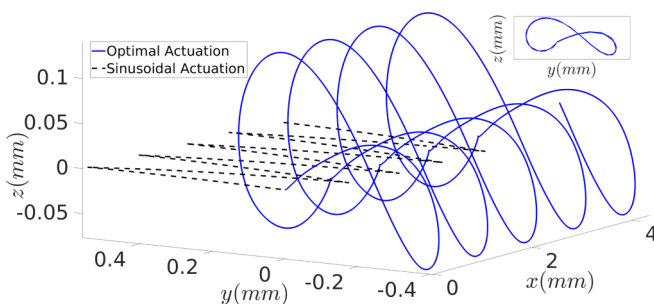
FIG. 5. Simulated trajectory of the head of the swimmer under both the optimal and sinusoidal field for 3 s of straight swimming under both actuation patterns. In the corner, the trajectory in the y-z plane.
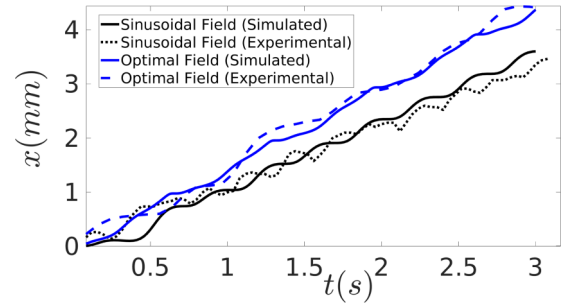
FIG. 6. Simulated and experimental horizontal displacements of the swimmer actuated by the optimal magnetic field and the sinusoidal magnetic field for 3 s of straight swimming under both actuation patterns.

V. EXPERIMENTAL RESULTS

The numerical solution of the optimal control problem (Fig. 4) is interpolated by its truncated Fourier expansion (first 10 modes) and then implemented in the magnetic generation system to actuate the swimmer. As predicted by the simulations, the optimal field out-performs the sinusoidal field in terms of horizontal propulsion speed, as shown in Fig. 6. Figure 7 shows the 3D trajectory of the experimental swimmer during one period. Figure 8 shows the deformation pattern undergone by the swimmer in the two perpendicular planes. Under optimal actuation, the swimmer reaches a mean horizontal propulsion speed of $1.54 \pm 0.3 \times 10^{-3}$ ms^{-1} ($N = 6$). The mean relative error (∞ norm) between the simulated and observed x displacement is $0.16(\pm 0.02)$.

We refer the reader to the supplemental movies [31] for a side-by-side comparison of the displacements of the swimmer actuated by the optimal and sinusoidal field.

VI. DISCUSSION

The optimization process exploits two time varying components of the field in order to maximize the horizontal speed of the swimmer, which allows the swimmer to perform a 3D trajectory. This swimming strategy shows the necessity of allowing flagellar swimmers to go out of plane in order to swim at a maximal propulsion speed, as illustrated in Fig. 5 and Fig. 7. The effectiveness of nonplanar actuation has been corroborated in the literature by studies where nonplanar helical waves have been shown to induce a faster propulsion speed for flagellar swimmers. For example, in Ref. [32], the spermlike swimmer's swimming speed increases between 1.2
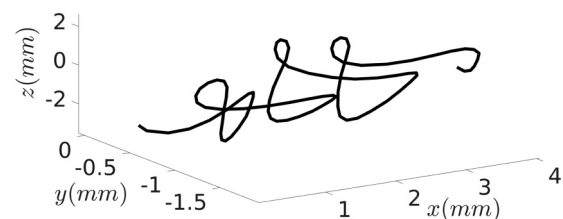
FIG. 7. Trajectory of the experimental swimmer actuated by the optimal magnetic field given in Fig. 4 during three periods of the magnetic field.
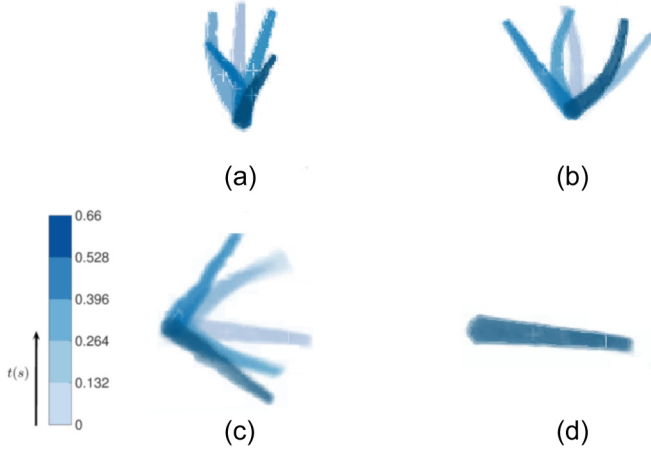
FIG. 8. Deformation pattern of the experimental swimmer actuated by the optimal magnetic field and the sinusoidal magnetic field over one period in two planes. (a) Optimal field, top view; (b) sinusoidal field, top view; (c) optimal field, side view; (d) sinusoidal field, side view. The snapshots of the experimental swimmer are taken at equal time steps over a period of the actuating fields. We observe (as expected) no deformation in the side plane for the sinusoidal field.

and 2 times (depending on the viscosity of the fluid) when switching between a planar swimming induced by sinusoidal actuation and helical swimming induced by a conical magnetic field. This characteristic is also shown in Ref. [33] for self-propelled swimmers. However, our work differs from these approaches as it does not rely on an *a priori* prescribed actuation pattern or shape deformation but optimizes the 3D driving magnetic field of the swimmer which allows the generation of swimmer-specific optimal actuation. From Fig. 6, we see that the dynamic model accurately predicts the horizontal displacements of the swimmer under both magnetic fields. It is less accurate in predicting the value of the amplitudes of the oscillations of the swimmer along the y and z axis as can be seen from comparing Figs. 7 and 5. However, the shapes of the predicted and experimental trajectories match qualitatively. The swimmer's displacements are characterized by the deformations of its tail, as a consequence of the forces and torques balances in Eq. (5). The experimental deformation patterns of the tail under both magnetic fields are shown in Fig. 8, which illustrates how the swimmer breaks the time-reversible symmetry of the Stokes flow to propel in both cases. In particular, the deformation pattern under the optimal field shows a torsion of the tail of the swimmer in addition to a beating pattern. This torsion of the tail causes the swimmer to go out of plane. This same effect of the torsion on the trajectory has been shown in the case of flagellated cells that self-propel along a 3D chiral path when the torsion of the flagellum is coupled with an oscillating waveform [34].

Although the main focus of this work was to optimize the speed of the flexible robot for swimming along a straight line, this swimming strategy is easily implementable for open loop or closed loop path following (see Ref. [20] for an example) by applying the static component of the magnetic field in the direction tangent to the curve, and the time-varying components in the normal and binormal directions.

VII. CONCLUSION

We have investigated the design of optimal actuation patterns for a flexible low-Reynold-number swimmer actuated by magnetic fields using a simple computationally inexpensive model that predicts the horizontal displacement of the swimmer. This provides an automated procedure for the optimal control design of flexible magnetic low-Reynolds-number swimmers. Using this approach, we simulate magnetic fields that maximize the horizontal propulsion speed of the swimmer. From this, we are able to propose a novel magnetic actuation pattern that allows the swimmer to swim significantly faster compared to the usual sinusoidal actuation. This actuation pattern is experimentally validated on a flexible low-Reynolds-number swimmer. The dynamic model used accurately predicts the horizontal displacement of the experimental swimmer under both the optimal and sinusoidal actuation. The simulation and experimental results show that it is necessary to go out of plane in order to maximize the propulsion speed of flexible magnetic low-Reynolds-number swimmers. Although the dynamic model used is limited in its accuracy, since it is based on an approximation of the fluid-structure interaction of the swimmer, this study showcases the usefulness of such a simplified model for computationally inexpensive control design for the actuation of flagellar magnetic swimmers. Current research is focused on finding a solution to allow propulsion of flagellated swimmers in confined environments [35,36] or in the presence of obstacles, such as the human vasculature [14]. For this purpose, the technique presented in this paper could be generalized to find magnetic fields that allows the propulsion of the robot in a confined environnement by adapting the model.

APPENDIX A: FORMULATION OF THE HYDRODYNAMICS OF THE SWIMMER

1. Parametrization of the rotation matrices and angular velocities

The rotation matrix R_{head} represents the coordinates transform between the world frame and $\mathcal{R}_{\text{head}}$. It is parametrized by three angles $(\theta_x, \theta_y, \theta_z)$ resulting from a Z-Y-X rotation sequence:

$$R_{\text{head}} = R_x(\theta_x)R_y(\theta_y)R_z(\theta_x), \qquad (A1)$$

where R_x, R_y, and R_z are the elementary rotation matrices around the x, y, and z axes.

Similarly, for each link i, the rotation matrix R_i represents the coordinates transform between the head's frame $\mathcal{R}_{\text{head}}$ and the frame associated with link i $\mathcal{R}_i$. It is parametrized by two angles (ϕ_y^i, ϕ_z^i) resulting from a Z-Y rotation sequence:

$$R_i = R_{\text{head}}\tilde{R}_i R_{\text{head}}^T \quad \text{for } i \in (1, \ldots, N). \qquad (A2)$$

where $\tilde{R}_i = R_y(\phi_y^i)R_z(\phi_z^i)$.

For all skew-symmetric matrix $A \in \mathbb{R}^{3 \times 3}$, we can define a vector $\boldsymbol{\Omega}$ verifying:

$$\forall V \in \mathbb{R}^3 \; AV = \boldsymbol{\Omega} \times V. \tag{A3}$$

Using this property, we define the following angular velocity vectors:

(i) $\boldsymbol{\Omega}_{\text{head}}$ is the vector defining the cross product associated with the skew-symmetric matrix $\dot{R}_{\text{head}} R_{\text{head}}^T$. $\boldsymbol{\Omega}_{\text{head}}$ depends linearly on $(\dot{\theta}_x, \dot{\theta}_y, \dot{\theta}_z)$ as follows:

$$\boldsymbol{\Omega}_{\text{head}} = L_{\text{head}} \begin{pmatrix} \dot{\theta}_x \\ \dot{\theta}_y \\ \dot{\theta}_z \end{pmatrix}, \tag{A4}$$

where

$$L_{\text{head}} = \begin{bmatrix} 1 & 0 & \sin(\theta_y) \\ 0 & \cos(\theta_x) & -\cos(\theta_y)\sin(\theta_x) \\ 0 & \sin(\theta_x) & \cos(\theta_x)\cos(\theta_y) \end{bmatrix}, \tag{A5}$$

(ii) $\boldsymbol{\Omega}_i$ is the vector defining the cross product associated with the skew-symmetric matrix $\dot{\tilde{R}}_i \tilde{R}_i^T$ for $i \in (1 \cdots N)$. $\boldsymbol{\Omega}_i$ depends linearly on $(\dot{\phi}_y^i, \dot{\phi}_z^i)$ as follows:

$$\boldsymbol{\Omega}_i = L_i \begin{pmatrix} \dot{\phi}_y^i \\ \dot{\phi}_z^i \end{pmatrix}, \tag{A6}$$

where

$$L_i = \begin{bmatrix} \sin(\phi_y^i) & 0 \\ \cos(\phi_y^i) & 0 \\ 0 & 1 \end{bmatrix}. \tag{A7}$$

2. Hydrodynamical force and torque on the head of the swimmer

We consider a drag force acting on the head of the swimmer that is proportional to its velocity in each direction of the head frame's $\mathcal{R}_{\text{head}}$ and a resistive torque proportional to the angular velocity of the head:

$$\boldsymbol{F}_{\text{head}}^h = -R_{\text{head}} \begin{pmatrix} k_{H,\parallel} & 0 & 0 \\ 0 & k_{H,\perp} & 0 \\ 0 & 0 & k_{H,\perp} \end{pmatrix} R_{\text{head}}^T \dot{\boldsymbol{X}}, \tag{A8}$$

$$\boldsymbol{T}_{\text{head}}^h = -k_R \boldsymbol{\Omega}_{\text{head}} = -k_R L_{\text{head}} \dot{\boldsymbol{\Theta}},$$

where $k_{H,\parallel}$ and $k_{H,\perp}$ are the parallel and perpendicular hydrodynamic coefficients of the head and k_R is a rotationnal drag coefficient.

3. Expression of the hydrodynamical force density on a point of the tail of the swimmer

For $i = (1 \cdots N)$, we consider a point $\boldsymbol{x}_i(s)$ on the ith link of the tail parametrized by its arclength s such as

$$\boldsymbol{x}_i(s) = \boldsymbol{O}_i - s\boldsymbol{e}_x^i. \tag{A9}$$

Using the rotation matrices defined in the previous paragraph, $\boldsymbol{x}_i(s)$ is written as:

$$\boldsymbol{x}_i(s) = \boldsymbol{O}_H - rR_{\text{head}}\boldsymbol{e}_x - l\sum_{k=1}^{i-1} R_{\text{head}}\tilde{R}_k\boldsymbol{e}_x - sR_{\text{head}}\tilde{R}_i\boldsymbol{e}_x, \tag{A10}$$

where r is the distance between $\boldsymbol{O}_H$ and $\boldsymbol{O}_i$. We differentiate the previous equation to obtain the expression of the velocity of $\boldsymbol{x}_i(s)$:

$$\dot{\boldsymbol{x}}_i(s) = \dot{\boldsymbol{X}} - r\dot{R}_{\text{head}}\boldsymbol{e}_x - l\sum_{k=1}^{i-1} \dot{R}_{\text{head}}\tilde{R}_k\boldsymbol{e}_x$$
$$- l\sum_{k=1}^{i-1} R_{\text{head}}\dot{\tilde{R}}_k\boldsymbol{e}_x - s\dot{R}_{\text{head}}\tilde{R}_i\boldsymbol{e}_x - sR_{\text{head}}\dot{\tilde{R}}_i\boldsymbol{e}_x. \tag{A11}$$

Following resistive force theory, the density of hydrodynamic force $\boldsymbol{f}_i$ is linear with respect to the components of $\dot{\boldsymbol{x}}_i(s)$:

$$\boldsymbol{f}_i(s) = -k_{\parallel}\big(\dot{\boldsymbol{x}}_i(s).\boldsymbol{e}_x^i\big)\boldsymbol{e}_x^i - k_{\perp}\big(\dot{\boldsymbol{x}}_i(s).\boldsymbol{e}_y^i\big)\boldsymbol{e}_y^i$$
$$- k_{\perp}\big(\dot{\boldsymbol{x}}_i(s).\boldsymbol{e}_z^i\big)\boldsymbol{e}_z^i$$
$$= S_i\dot{\boldsymbol{x}}_i(s), \tag{A12}$$

where $k_{\parallel}$ and $k_{\perp}$ are respectively the parallel and prependicular drag coefficients of the swimmer's tail and, for each link i:

$$S_i = (R_{\text{head}}\tilde{R}_i)D(R_{\text{head}}\tilde{R}_i)^T, \tag{A13}$$

where

$$D = -\begin{pmatrix} k_{\parallel} & 0 & 0 \\ 0 & k_{\perp} & 0 \\ 0 & 0 & k_{\perp} \end{pmatrix}. \tag{A14}$$

Using the expression of $\dot{\boldsymbol{x}}_i(s)$ [Eq. (A11)] in Eq. (A12), the hydrodynamic force density reads:

$$\boldsymbol{f}_i(s) = S_i\dot{\boldsymbol{X}} - r\big(R_{\text{head}}\tilde{R}_i D\tilde{R}_i^T\big)R_{\text{head}}^T\dot{R}_{\text{head}}\boldsymbol{e}_x$$
$$- l\big(R_{\text{head}}\tilde{R}_i D\tilde{R}_i^T\big)\sum_{k=1}^{i-1} R_{\text{head}}^T\dot{R}_{\text{head}}\tilde{R}_k\boldsymbol{e}_x$$
$$- l\big(R_{\text{head}}\tilde{R}_i D\tilde{R}_i^T\big)\sum_{k=1}^{i-1} \tilde{R}_k\tilde{R}_k^T\dot{\tilde{R}}_k\boldsymbol{e}_x$$
$$- s\big(R_{\text{head}}\tilde{R}_i D\tilde{R}_i^T\big)R_{\text{head}}^T\dot{R}_{\text{head}}\tilde{R}_i\boldsymbol{e}_x$$
$$- s\big(R_{\text{head}}\tilde{R}_i D\tilde{R}_i^T\big)\dot{\tilde{R}}_i\boldsymbol{e}_x. \tag{A15}$$

Using the definition of the angular velocity vectors [Eqs. (A4) and (A6)], we rewrite the expression above as:

$$\boldsymbol{f}_i(s) = S_i\dot{\boldsymbol{X}} - r\big(R_{\text{head}}\tilde{R}_i D\tilde{R}_i^T\big)\boldsymbol{\Omega}_{\text{head}} \times \boldsymbol{e}_x$$
$$- l\big(R_{\text{head}}\tilde{R}_i D\tilde{R}_i^T\big)\sum_{k=1}^{i-1} \boldsymbol{\Omega}_{\text{head}} \times (\tilde{R}_k\boldsymbol{e}_x)$$
$$- l\big(R_{\text{head}}\tilde{R}_i D\tilde{R}_i^T\big)\sum_{k=1}^{i-1} \tilde{R}_k\boldsymbol{\Omega}_k \times \boldsymbol{e}_x$$
$$- s\big(R_{\text{head}}\tilde{R}_i D\tilde{R}_i^T\big)\boldsymbol{\Omega}_{\text{head}} \times (\tilde{R}_i\boldsymbol{e}_x)$$
$$- s(R_{\text{head}}\tilde{R}_i D)\boldsymbol{\Omega}_i \times \boldsymbol{e}_x. \tag{A16}$$

In order to write cross products in matricial form, we introduce the following notation:

$$\forall V = \begin{pmatrix} V_1 & V_2 & V_3 \end{pmatrix}^T \in \mathbb{R}^3 \; [V]^\times = \begin{pmatrix} 0 & -V_3 & V_2 \\ V_3 & 0 & -V_1 \\ -V_2 & V_1 & 0 \end{pmatrix}.$$

(A17)

Using this notation and the linear dependency of $\boldsymbol{\Omega_{\text{head}}}$ and $\boldsymbol{\Omega_i}$ on the angular velocities [Eqs. (A4) and (A6)], the hydrodynamical drag force density on link i is written as a linear function of $\dot{X}$, $\boldsymbol{\Omega}$, and $\dot{\boldsymbol{\Phi}}$:

$$\boldsymbol{f_i}(s) = A^i(s) \begin{pmatrix} \dot{X} \\ \dot{\boldsymbol{\Theta}} \\ \dot{\boldsymbol{\Phi}} \end{pmatrix},$$

(A18)

where $A^i(s) \in \mathbb{R}^{3,2N+6}$ is defined blockwise as:

$$A^i(s) = \begin{pmatrix} A_X^i \in \mathbb{R}^{3\times3} \\ A_\theta^i \in \mathbb{R}^{3\times3} \\ A_1^i \in \mathbb{R}^{2\times3} \\ \vdots \\ A_N^i \in \mathbb{R}^{2\times3} \end{pmatrix},$$

(A19)

where

$$\begin{cases} A_X^i(s) = S_i \\ A_\theta^i(s) = \left(R_{\text{head}}\tilde{R}_i D\tilde{R}_i^T\right)\left[re_x + l\sum_{k=1}^{i-1}\tilde{R}_k e_x \right]^\times L_{\text{head}} \\ \qquad\quad + \left(R_{\text{head}}\tilde{R}_i D\tilde{R}_i^T\right)[s\tilde{R}_i e_x]^\times L_{\text{head}} \\ A_1^i(s) = l\left(R_{\text{head}}\tilde{R}_i D\tilde{R}_i^t\right)\tilde{R}_1[e_x]^\times L_1 \\ \qquad\vdots \\ A_{i-1}^i(s) = l\left(R_{\text{head}}\tilde{R}_i D\tilde{R}_i^t\right)\tilde{R}_{i-1}[e_x]^\times L_{i-1} \\ A_i^i(s) = s(R_{\text{head}}\tilde{R}_i D)[e_x]^\times L_i \\ A_j^i = 0_3 \;\; \forall j > i \end{cases}$$

(A20)

4. Hydrodynamical forces and torques on each link

We define the two $3 \times 2N + 6$ matrices B^i and C^i as follows:

$$\begin{cases} B^i = \displaystyle\int_0^l A^i(s)ds \\ C^i = \displaystyle\int_0^l sA^i(s)ds \end{cases}.$$

(A21)

Using this notation, the hydrodynamical force on link i depends linearly on the position and shape velocities as follows:

$$\boldsymbol{F_i^h} = B^i \begin{pmatrix} \dot{X} \\ \dot{\boldsymbol{\Theta}} \\ \dot{\boldsymbol{\Phi}} \end{pmatrix}.$$

(A22)

The hydrodynamic torque on link i calculated about the point O_H is computed from the hydrodynamical force density as follows:

$$\boldsymbol{T_{i,H}^h} = \int_0^l (\boldsymbol{x_i}(s) - \boldsymbol{O_H}) \times \boldsymbol{f_i}(s)ds.$$

(A23)

We rewrite $(\boldsymbol{x_i}(s) - \boldsymbol{O_H})$ as:

$$(\boldsymbol{x_i}(s) - \boldsymbol{O_H}) = -rR_{\text{head}}e_x - \sum_{k=1}^{i-1} lR_{\text{head}}\tilde{R}_k e_x - sR_{\text{head}}\tilde{R}_i e_x.$$

(A24)

$\boldsymbol{T_{i,H}^h}$ is then expressed as:

$$\boldsymbol{T_{i,H}^h} = -\left[rR_{\text{head}}e_x + \sum_{k=1}^{i-1} lR_{\text{head}}\tilde{R}_k e_x \right]^\times \int_0^l \boldsymbol{f_i}(s)ds$$
$$- [R_{\text{head}}\tilde{R}_i]^\times \int_0^l s\boldsymbol{f_i}(s)ds.$$

(A25)

Thus, the matricial form of $\boldsymbol{T_{i,H}^h}$ is

$$\boldsymbol{T_{i,H}^h} = -\left(\left[rR_{\text{head}}e_x + \sum_{k=1}^{i-1} lR_{\text{head}}\tilde{R}_k e_x \right]^\times B^i \right) \begin{pmatrix} \dot{X} \\ \dot{\boldsymbol{\Theta}} \\ \dot{\boldsymbol{\Phi}} \end{pmatrix}$$
$$- ([R_{\text{head}}\tilde{R}_i]^\times C^i) \begin{pmatrix} \dot{X} \\ \dot{\boldsymbol{\Theta}} \\ \dot{\boldsymbol{\Phi}} \end{pmatrix}.$$

(A26)

Similarly, for $k = (i, \dots, N)$, the hydrodynamic torque on link i about O_k reads:

$$\boldsymbol{T_{i,j}^h} = -\left(\sum_{k=j}^{i-1}[lR_{\text{head}}\tilde{R}_k e_x]^\times B^i - [R_{\text{head}}\tilde{R}_i]^\times C^i\right) \begin{pmatrix} \dot{X} \\ \dot{\boldsymbol{\Theta}} \\ \dot{\boldsymbol{\Phi}} \end{pmatrix}.$$

(A27)

5. Equations of motion

Using the expressions of the hydrodynamical forces and torques in the previous section Eqs. (A22), (A26), and (A27)], the left-hand side of the dynamical system (7) is written as a linear function of the state derivatives:

$$\begin{pmatrix} \sum_{i=1}^N \boldsymbol{F_i^h} + \boldsymbol{F_{\text{head}}^h} \\ \boldsymbol{T_{\text{head}}^h} + \sum_{i=1}^N \boldsymbol{T_{i,H}^h} \\ (\sum_{i=1}^N \boldsymbol{T_{i,H}^h}) \cdot \boldsymbol{e_y^1} \\ (\sum_{i=1}^N \boldsymbol{T_{i,H}^h}) \cdot \boldsymbol{e_z^1} \\ \vdots \\ \sum_{i=k}^N \boldsymbol{T_{i,k}^h} \cdot \boldsymbol{e_y^k} \\ \sum_{i=k}^N \boldsymbol{T_{i,k}^h} \cdot \boldsymbol{e_z^k} \\ \vdots \\ \boldsymbol{T_{N,N}^h} \cdot \boldsymbol{e_y^N} \\ \boldsymbol{T_{N,N}^h} \cdot \boldsymbol{e_z^N} \end{pmatrix} = M^h(\boldsymbol{\Theta}, \boldsymbol{\Phi}) \begin{pmatrix} \dot{X} \\ \dot{\boldsymbol{\Theta}} \\ \dot{\boldsymbol{\Phi}} \end{pmatrix},$$

(A28)

where $M^h \in \mathbb{R}^{2N+6\times 2N+6}$ is defined by blocks as:

$$M^h = \begin{pmatrix} M^X \in \mathbb{R}^{3\times2N+6} \\ M^\Theta \in \mathbb{R}^{3\times2N+6} \\ M^1 \in \mathbb{R}^{2\times2N+6} \\ \vdots \\ M^N \in \mathbb{R}^{2\times2N+6} \end{pmatrix},$$

(A29)
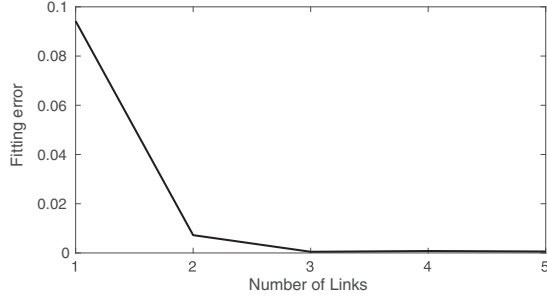
FIG. 9. Fitting error in function of the number of links of the model.

where

$$
\begin{cases}
M^X = -\left(R_{\text{head}} D_H R_{\text{head}}^T \ 0_3 \ O_{3,2\times N}\right) + \sum_{i=1}^{N} B^i \\[2mm]
M^{\Theta} = -k_R\left(0_3 \ L_{\text{head}} \ O_{3,3\times N}\right) \\[1mm]
\qquad\quad - \sum_{i=1}^{N}\left[R_{\text{head}}\left(r e_x + \sum_{k=1}^{i-1} l\tilde{R}_k e_x\right)\right]^{\times} B^i \\[2mm]
\qquad\quad - \sum_{i=1}^{N}[R_{\text{head}}\tilde{R}_i]^{\times} C^i \\[2mm]
M^1 = -R_1^* \sum_{i=1}^{N}\left(\sum_{k=1}^{i-1}[lR_{\text{head}}\tilde{R}_k e_x]^{\times} B^i\right) \\[2mm]
\qquad\quad - R_1^* \sum_{i=1}^{N}[R_{\text{head}}\tilde{R}_i]^{\times} C^i \\[1mm]
\qquad\quad \vdots \\[1mm]
M^N = -R_N^* \sum_{k=1}^{N-1}([lR_{\text{head}}\tilde{R}_k e_x]^{\times} B^N) \\[2mm]
\qquad\quad - R_N^*[R_{\text{head}}\tilde{R}_N]^{\times} C^N
\end{cases}
\qquad (A30)
$$

TABLE I. Parameters used for the sperm cell simulations.

Parameter	Value
Length of the tail	$L = 7$ mm
Radius of the head	$r = 0.3$ mm
Parallel resistive coefficient, head	$k_{H,\parallel} = 1.15\,\mathrm{N\,s\,(m^{-1})}$
Perpendicular resistive coefficient, head	$k_{H,\perp} = 4.37\,\mathrm{N\,s\,(m^{-1})}$
Rotational resistive coefficient, head	$k_{H,R} = 0.6\,\mathrm{N\,m\,s}$
Parallel resistive coefficient, tail	$k_{T,\parallel} = 0.35\,\mathrm{N\,s\,(m^{-1})}$
Perpendicular resistive coefficient, tail	$k_{T,\perp} = 0.813\,\mathrm{N\,s\,(m^{-1})}$
Elastic coefficient	$k_{el} = 8.678 10^{-7}\,\mathrm{N\,m^{-1}}$
Magnetization	$M = 1.685 10^{-4}\,\mathrm{A\,m^{-1}}$

where R_i^* is the 2×3 matrix consisting of the second and third line of the matrix $(R_{\text{head}}\tilde{R}_i)^T$ which represents the projection on the plane (e_y^i, e_z^i).

APPENDIX B: SIMULATION PARAMETERS

Table I shows the numerical values of the fitted parameters of the model.

APPENDIX C: FITTING ERROR AND NUMBER OF LINKS

Figure 9 shows the result of the parameter fitting (relative l^2 norm) between the experimental velocity-frequency response curve and the simulated velocity-frequency response curve. As seen in the figure, the model fails to accurately match the experimental velocity-frequency curve with $N = 1$ and $N = 2$ links. The fitting results in a small error for $N \geqslant 3$.

[1] B. J. Nelson, I. K. Kaliakatsos, and J. J. Abbott, Microrobots for minimally invasive medicine, Annu. Rev. Biomed. Eng. **12**, 55 (2010).

[2] M. Sitti, H. Ceylan, W. Hu, J. Giltinan, M. Turan, S. Yim, and E. D. Diller, Biomedical applications of untethered mobile milli/microrobots, Proc. IEEE **103**, 205 (2015).

[3] F. Qiu, S. Fujita, R. Mhanna, L. Zhang, B. R. Simona, and B. J. Nelson, Magnetic helical microswimmers functionalized with lipoplexes for targeted gene delivery, Adv. Funct. Mater. **25**, 1666 (2015).

[4] D. Patra, S. Sengupta, W. Duan, H. Zhang, R. Pavlick, and A. Sen, Intelligent, self-powered, drug delivery systems, Nanoscale **5**, 1273 (2013).

[5] M. J. Mack, Minimally invasive and robotic surgery, J. Am. Med. Assoc. **285**, 568 (2001).

[6] S. Fusco, Mahmut S. Sakar, S. Kennedy, C. Peters, R. Bottani, F. Starsich, A. Mao, G. A. Sotiriou, S. Pané, S. E. Pratsinis *et al.*, An integrated microrobotic platform for on-demand, targeted therapeutic interventions, Adv. Mater. **26**, 952 (2014).

[7] W. Gao, D. Kagan, On S. Pak, C. Clawson, S. Campuzano, E. Chuluun-Erdene, E. Shipton, E. E. Fullerton, L. Zhang, E. Lauga, and J. Wang, Cargo-towing fuel-free magnetic nanoswimmers for targeted drug delivery, Small **8**, 460 (2012).

[8] E. Lauga and T. R. Powers, The hydrodynamics of swimming microorganisms, Rep. Prog. Phys. **72**, 096601 (2009).

[9] T. Qiu, T.-C. Lee, A. G. Mark, K. I. Morozov, R. Münster, O. Mierka, S. Turek, A. M. Leshansky, and P. Fischer, Swimming by reciprocal motion at low reynolds number, Nat. Commun. **5**, 11 (2014).

[10] A. F. Tabak and S. Yesilyurt, Computationally-validated surrogate models for optimal geometric design of bio-inspired swimming robots: Helical swimmers, Comput. Fluids **99**, 190 (2014).

[11] A. Barbot, D. Decanini, and G. Hwang, The rotation of micro-robot simplifies 3d control inside microchannels, Sci. Rep. **8**, 438 (2018).

[12] R. Dreyfus, J. Baudry, M. L. Roper, M. Fermigier, H. A. Stone, and J. Bibette, Microscopic artificial swimmers, Nature **437**, 862 (2005).

[13] I. S. M. Khalil, H. C. Dijkslag, L. Abelmann, and S. Misra, Magnetosperm: A microrobot that navigates using weak magnetic fields, Appl. Phys. Lett. **104**, 223701 (2014).

[14] B. Jang, A. Aho, B. J. Nelson, and S. Pane, Fabrication and locomotion of flexible nanoswimmers, in *Proceedings of the IEEE/RSJ International Conference on Intelligent Robots and Systems (IROS'18)* (IEEE, Madrid, 2018).

[15] S. Kim, S. Lee, J. Lee, B. J. Nelson, L. Zhang, and H. Choi, Fabrication and manipulation of ciliary microrobots with non-reciprocal magnetic actuation, Sci. Rep. **6**, 30713 (2016).

[16] X. Ma, S. Jang, M. N. Popescu, W. E. Uspal, A. Miguel-López, K. Hahn, D.-P. Kim, and S. Sánchez, Reversed Janus micro/nanomotors with internal chemical engine, ACS Nano **10**, 8751 (2016).

[17] B. Jang, A. Hong, H. E. Kang, C. Alcantara, S. Charreyron, F. Mushtaq, E. Pellicer, R. Büchel, J. Sort, S. S. Lee *et al.*, Multiwavelength light-responsive Au/B-TiO$_2$ Janus micromotors, ACS Nano **11**, 6146 (2017).

[18] D. Ahmed, T. Baasch, B. Jang, S. Pane, J. Dual, and B. J. Nelson, Artificial swimmers propelled by acoustically activated flagella, Nano Lett. **16**, 4968 (2016).

[19] T. Xu, J. Yu, X. Yan, H. Choi, and L. Zhang, Magnetic actuation based motion control for microrobots: An overview, Micromachines **6**, 1346 (2015).

[20] A. Oulmas, N. Andreff, and S. Régnier, 3d closed-loop motion control of swimmer with flexible flagella at low reynolds numbers, in *Proceedings of the 2017 IEEE/RSJ International Conference on Intelligent Robots and Systems (IROS'17)* (IEEE, Los Alamitos, CA, 2017), pp. 1877–1882.

[21] J. J. Abbott, K. E. Peyer, Marco C. Lagomarsino, L. Zhang, L. Dong, I. K. Kaliakatsos, and B. J. Nelson, How should microrobots swim? Int. J. Robot. Res. **28**, 1434 (2009).

[22] J. Gray and G. J. Hancock, The propulsion of sea-urchin spermatozoa, J. Exp. Biol. **32**, 802 (1955).

[23] B. M. Friedrich, I. H. Riedel-Kruse, J. Howard, and F. Jülicher, High-precision tracking of sperm swimming fine structure provides strong test of resistive force theory, J. Exp. Biol. **213**, 1226 (2010).

[24] C. Moreau, L. Giraldi, and H. A. B. Gadelha, The asymptotic coarse-graining formulation of slender-rods, bio-filaments and flagella, J. R. Soc. Interface **15**, 20180235 (2018).

[25] F. Alouges, A. DeSimone, L. Giraldi, and M. Zoppello, Self-propulsion of slender micro-swimmers by curvature control: N-link swimmers, Int. J. Non Linear Mech. **56**, 132 (2013).

[26] F. Alouges, A. DeSimone, L. Giraldi, and M. Zoppello, Can magnetic multilayers propel artificial microswimmers mimicking sperm cells? Soft Robot. **2**, 117 (2015).

[27] P. Falugi, E. C. Kerrigan, and E. V. Wyk, Imperial College London Optimal Control Software (ICLOCS), http://www.ee.ic.ac.uk/ICLOCS, 2010.

[28] E. Marchand, F. Spindler, and F. Chaumette, Visp for visual servoing: A generic software platform with a wide class of robot control skills, IEEE Robot. Autom. Mag. **12**, 40 (2005).

[29] T. Xu, Propulsion characteristics and visual servo control of scaled-up helical microswimmers, Ph.D. thesis, Université Pierre et Marie Curie-Paris VI, 2014.

[30] G. T. Yates, How microorganisms move through water: The hydrodynamics of ciliary and flagellar propulsion reveal how microorganisms overcome the extreme effect of the viscosity of water, Am. Sci. **74**, 358 (1986).

[31] See Supplemental Material at http://link.aps.org/supplemental/10.1103/PhysRevE.101.042604 for the movies showing the trajectory of the swimmer under both fields.

[32] I. S. M. Khalil, A. F. Tabak, M. A. Seif, A. Klingner, and M. Sitti, Controllable switching between planar and helical flagellar swimming of a soft robotic sperm, PloS ONE **13**, e0206456 (2018).

[33] A. T. Chwang and T. Y. Wu, A note on the helical movement of micro-organisms, Proc. R. Soc. Lond. B **178**, 327 (1971).

[34] J. F. Jikeli, L. Alvarez, B. M. Friedrich, L. G. Wilson, R. Pascal, R. Colin, M. Pichlo, A. Rennhack, C. Brenker, and U. B. Kaupp, Sperm navigation along helical paths in 3d chemoattractant landscapes, Nat. Commun. **6**, 7985 (2015).

[35] K. Ishimoto and E. A. Gaffney, A study of spermatozoan swimming stability near a surface, J. Theor. Biol. **360**, 187 (2014).

[36] H. Shum and E. A. Gaffney, Hydrodynamic analysis of flagellated bacteria swimming in corners of rectangular channels, Phys. Rev. E **92**, 063016 (2015).